Technische Universität München
Fakultät für Physik

Abschlussarbeit im Bachelorstudiengang Physik

Test eines IROC GEM-Prototypen mit niederenergetischen Protonen

Test of an IROC GEM prototype with low energy protons

Andreas Mathis

31. Juli 2013

Erstgutachter (Themensteller): Prof. L. Fabbietti
Zweitgutachter: Prof. L. Oberauer

Betreuer: Dr. P. Gasik

Contents

Introduction

The ALICE[1] experiment is located at the LHC[2] at CERN[3]. It is a dedicated heavy-ion detector to study Pb–Pb collisions at a center-of-mass energy of 5.5 TeV per nucleon pair [1]. In its central barrel, the Time Projection Chamber is the main detector for tracking. The TPC is read out by Multi Wire Proportional Chambers (MWPC) operated in gated mode to reduce the number of ions drifting back to the active volume of the detector. The gating grid is operated with a frequency of 1 kHz strongly limiting the rate of data taking.

After the upgrade during the second Long Shutdown (LS2) in 2018, the luminosity of the LHC will be increased. To to fulfil the new requirements, the ALICE TPC is planning a major upgrade. The existing MWPC readout will be replaced with GEM (Gas Electron Multiplier) based detectors to overcome the rate limitations of the gating grid.

A first prototype of the Inner Read-Out Chamber (IROC) was equipped with three GEM foils as an amplification stage and extensively tested during a test beam campaign at CERN. During three weeks of operation in the p-Pb beamtime in January 2013, 21 discharges occurred in the detector questioning the stable operation under LHC conditions.

One of the reasons for the high discharge rate might be slow, highly ionizing fragments produced in the supporting structure of the TPC during heavy ion collisions. To simulate these conditions, the IROC-prototype has been tested with low-energy protons at MLL (Mayer-Leibniz-Laboratorium). The stability of the chamber has been tested for different HV-settings of the GEMs and beam currents in a highly ionizing environment.

This Bachelor thesis describes the building and commissioning of the IROC-prototype and the experimental setup. Furthermore it presents the results of a simulation carried out as a preparation for the test beam and first results obtained in the laboratories and during the test beam.

[1] A Large Ion Collider Experiment
[2] Large Hadron Collider
[3] Conseil Européen pour la Recherche Nucléaire

Chapter 1

Principles of a GEM TPC

The principles of gaseous detectors are based on the direct collection of the ionization electrons produced by a charged particle traversing the gas medium. Although already invented during the first half of the last century, they still are very important and efficient tools for track reconstruction and particle identification.

1.1 Time Projection Chamber

A Time Projection Chamber (TPC) [2] is a gas detector used in particle physics for the three-dimensional reconstruction of tracks of charged particles in the gas volume. Figure 1.1 shows a schematic sketch of a TPC.

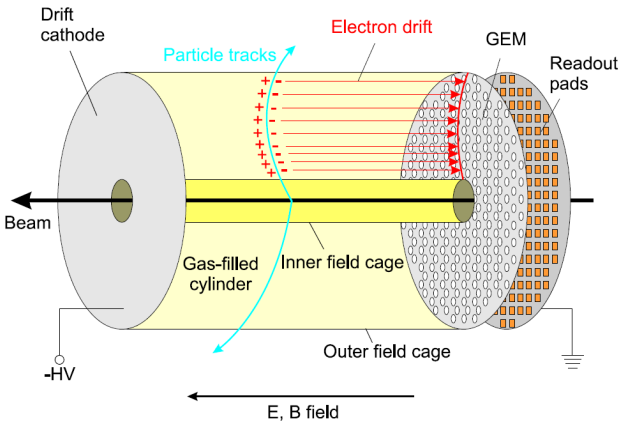

Figure 1.1: Schematic sketch of a TPC [3].

A typical TPC consists of a gas-filled, usually cylindrical, volume with a high voltage electrode in the center and anodes with a readout system on both end-plates, but also TPCs with different geometries have been built [4].

The beam pipe usually goes through the rotation axis of the TPC with the interaction point in its center. A TPC normally covers almost 4π of the solid angle. Gas

mixtures used in a TPCs usually consist of 90% of a noble gas (Ne, Ar, Xe) and 10% of a quencher (CO_2, CF_4, etc.) but also other mixtures or ratios are possible [5]. By applying high voltage to the drift cathode, a uniform electric field is created along the beam axis.

In order to obtain a good spatial resolution, the electric field inside the TPC has to be highly homogeneous. This is achieved by a so-called "field cage", which consists of a series of field strips surrounding the cylindrical volume. The strips divide the potential from the cathode stepwise down to the anode to minimize distortions of the drift field.

Also a parallel magnetic field is applied to bend the particle trajectories for momentum measurements. A positive side effect of the magnetic field is the suppression of the transversal diffusion of the drifting electrons thus improving the spatial resolution of the detector.

When a particle traverses the gas volume, the gas atoms are ionized along its path. Due to the electric field in the vessel, the charge is separated: the electrons drift to the anode whereas the ions drift to the central cathode where they are collected.

Since the signal induced by the primary electrons on the anode would be very small, multiplication is necessary to amplify the electrons drifting to the anode. This can be done for example with Multi-Wire Proportional Chambers [6] or, as discussed here, with Gas Electron Multipliers (see Section 1.2).

The measurement on the segmented anode gives the x and y coordinates of the track. Since the drift velocity of electrons is known and measured very precisely, with proper knowledge of the moment of the initial collision, the z-coordinate of the track can be determined as well. This allows a full reconstruction of the track. Together with $\mathrm{d}E/\mathrm{d}x$ measurements and momentum measurements in the magnetic field, full particle identification (PID) can be done in a TPC.

1.1.1 The ALICE TPC

With an active volume of $88\,\mathrm{m}^3$ and a total length of $5\,\mathrm{m}$ [1] the the ALICE TPC is the largest detector of this type in the world. It is the main tracking detector in the ALICE central barrel. Figure 1.2 shows a picture of the ALICE detector with the TPC.

Designed for high multiplicities ($\mathrm{d}N/\mathrm{d}y = 8000$), its spatial resolution is $300\,\mu\mathrm{m}$ and its $\mathrm{d}E/\mathrm{d}x$ resolution is 5-7% [7]. The TPC is operated with a $100\,\mathrm{kV}$ potential applied to the central cathode resulting in a constant drift field of $400\,\mathrm{V/cm}$ throughout the whole detector volume.

With the used gas mixture of Ne/CO_2 (90/10) the maximum drift time is $88\,\mu\mathrm{s}$. The MWPCs are running with a gain of around $7\text{-}8 \times 10^3$ [1].

The drift volume is defined by inner and outer fieldcage vessels with radii between $0.85\,\mathrm{m}$ and $2.47\,\mathrm{m}$ [7].

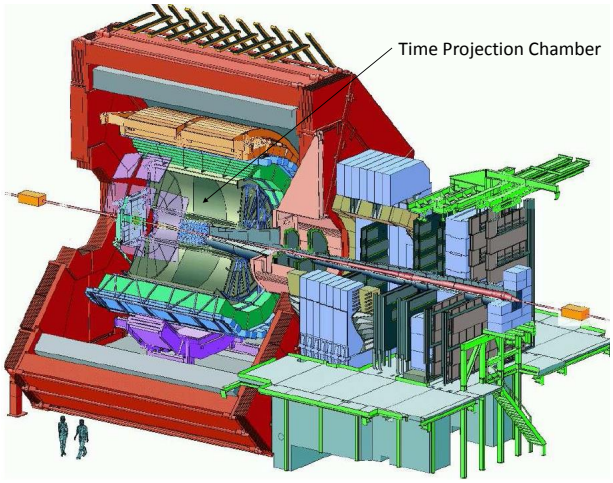

Figure 1.2: Artistic view of the ALICE detector with the TPC in its center [8].

At both ends, the readout chambers are positioned in the endplate of the TPC. The readout chambers are arranged in 18 sectors each covering 20° in azimuthal angle [1]. These chambers are subdivided into inner (IROC - Inner Read Out Chamber) and outer (OROC - Outer Read Out Chamber) chambers, thus accounting to 72 units [7].

1.2 GEM – Gas Electron Multiplier

As already mentioned, the signals of the primary electrons are not sufficient to induce a readable signal on the anode pad plane. Consequently, electron amplification is a crucial parameter for the operation of a gas detector like a TPC.

One technique for electron multiplication is the usage of GEM (Gas Electron Multiplier) [9] consisting of a 50 µm thin Kapton foil with a copper clad of 5 µm on both sides. The foil is perforated by photo-lithographic processing, forming a dense, regular pattern of holes. The holes have a pitch of 140 µm and a double conical shape with an inner diameter of 50 µm and an outer diameter of 70 µm. Figure 1.3 shows an electron microscope image of a GEM-foil.

For the electron amplification, a moderate potential difference of 300 - 400 V is applied between the two copper electrodes.

The field lines are focused in the double conical holes (see Figure 1.4) [10]. Thus, the resulting electric fields in the GEM holes are very high and can reach up to 50 kV/cm [11]. In this field the electrons are accelerated and thus ionize further gas atoms. The electrons created in a hole are extracted to the next amplification stage

or to the anode, whereas the ions are following the electric field lines and can either recombine on the cathode-side of a GEM foil or flow back into the drift volume of the detector.

The fields between two GEMs in the stack are from here on referred to as transfer fields and the field between the last GEM and the anode as induction field.

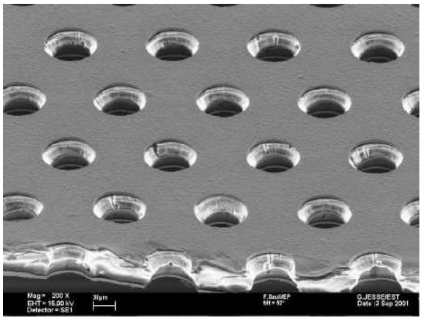

Figure 1.3: Close view of a GEM, taken with an electron microscope [12].

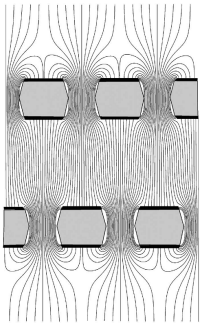

Figure 1.4: Schematics of the field-lines of a double-GEM [10].

One example for the successful employment of GEM-based detectors are the trackers for the COMPASS[1] [12] experiment at the SPS[2] at CERN. COMPASS is a fixed-target experiment using a 100 - 190 GeV polarized muon beam with a large intensity of $\sim 5 \times 10^7$ particles per second. The GEM detectors are operated at a gain of $\sim 10^4$.

1.2.1 Limitations of the GEM-technology

1.2.1.1 Ion Backflow

The so-called *Ion Backflow (IB)* is a commonly used quantity to describe the suppression of back drifting ions, defined as the ratio of the number of ions arriving at the cathode to the number of electrons arriving at the anode [13].

With triple GEM-stacks, the ion backflow into the active volume can be suppressed down to values of the percent level [14]. Nevertheless, the suppression of backdrifting ions for continuously operating GEM-based detectors is not as efficient as it is for detectors operating behind a gating grid [13], where the *IB* can reach the level of 10^{-5}. Contrary to fast electrons with a drift velocity of the order of cm/µs, the drift velocity of ions is three to four orders of magnitude smaller [15]. These slowly drifting ions lead to a slow buildup of space charge in the chamber disturbing the

[1] COmmon Muon and Proton Apparatus for Structure and Spectroscopy
[2] Super Proton Synchrotron

drift field and thus the spatial resolution of the detector. Still, a proper calibration with e.g. a laser system can resolve this issue [15].

So far, the above mentioned laser calibration was done offline, not online, which is much more challenging. One example for the offline calibration of a TPC is the system used for the STAR[3] TPC [16] at RHIC[4].

1.2.1.2 Discharges

Another problem is that in modern detectors GEMs are operated at extreme conditions, such as high counting rates and gas gains. This and additionally the presence of highly ionizing particles drastically increases the probability of discharges [17].

The physical limit for the gain in parallel plate detectors is the *Raether limit* [18]. For a critical total charge of $\sim 10^8$ electrons, discharges are very likely to occur. A similar situation is expected for GEM detectors with a total number of electrons in the avalanche of the order of

$$Q_{crit} \sim 10^6 - 10^7 \text{electrons [19]}. \tag{1.1}$$

Due to the enhanced diffusion in double or triple GEM-stacks, the electron cloud expands resulting in a lower charge density. This lowers the discharge probability and thus allows higher gains in multiple GEM-stacks [20] compared to single GEMs.

At very high induction and transfer fields, a discharge can propagate between several GEMs in the stack or even to the pad plane, which can cause severe damage to the Front End Electronics.

1.2.2 HV-settings

The achievable gain and ion backflow suppression depends strongly on the electric field in the GEM holes and on the transfer and induction fields.

Two different types of HV settings were used during the measurements with the prototype. The potentials are applied via resistor chains.

Standard settings The so-called standard settings are inherited from the COMPASS experiment [12] where GEM detectors are operated in a Ar/CO_2 (70/30) gas mixture.

Table 1.1 shows the HV-configuration for the unscaled standard setting. One notable fact is that the transfer fields are the same throughout the whole triple GEM-stack. For the ALICE TPC, all fields are scaled down by a factor given in percent.

[3] Solenoidal Tracker At RHIC
[4] Relativistic Heavy Ion Collider

Electrode	**Potential difference** (V)	**Field** (kV/cm)
GEM1	400	
Transfer field 1		3.73
GEM2	365	
Transfer field 2		3.73
GEM3	320	
Induction field		3.73

Table 1.1: Voltages and fields for standard setting, 100%.

Electrode	**Potential difference** (V)	**Field** (kV/cm)
GEM1	225	
Transfer field 1		3.8
GEM2	235	
Transfer field 2		0.2
GEM3	285	
Induction field		3.8

Table 1.2: Voltages and fields for IBF setting.

These standard settings were optimized for maximum stability against discharges. At 100% scaling factor, the standard setting in Ar/CO_2 (70/30) corresponds to a gain of $\sim 10^4$.

Experience has shown that the most stable configuration can be achieved with the highest amplification (highest ΔV) in the top GEM and lowest in the bottom. On the other hand, the ion backflow suppression of the standard HV-settings is rather poor.

Ion backflow (IBF) settings The so called IBF settings have been optimized to minimize the number of backdrifting ions. They were obtained in a set of measurements performed at TUM E18 laboratories. The main feature of this HV-setting is a high asymmetry between the transfer and the induction fields. This specific configuration of the fields (see Table 1.2) and the fact that the main amplification takes place in the last foil of the stack efficiently suppresses the amount of backdrifting ions down to a level of 5 % [21].

It should be noted, that the IBF configuration of the HV settings, contrary to the standard settings, may lead to the stability problems and increased discharge probability.

Chapter 2

The IROC-detector prototype

This chapter focuses on the assembly of the IROC-prototype.

2.1 GEM-foils

The GEM foils used for the ALICE GEM TPC prototype are manufactured at CERN in a single-mask process [22]. Although this process is less precise than the double-mask process, it is unavoidable due to the large size of the foils. The top side of the foil is divided into 18 sectors (compare Figure 2.1), whereas the bottom side is not segmented. The segmentation is necessary in order to keep the total charge that might be freed during a discharge as small as possible to prevent the foils from being damaged. For a constant capacitance of all sectors, the area is $\sim$100 cm^2 each. The foils are standard GEM foils as described in Section 1.2.

Figure 2.2 shows a drawing of the foils used to build the detector.

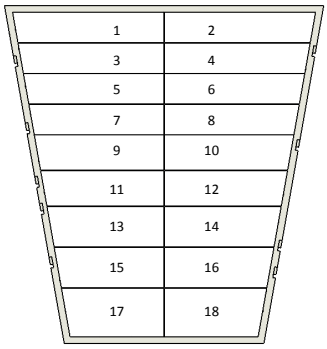

Figure 2.1: Numbering of the GEM-sectors (top view).

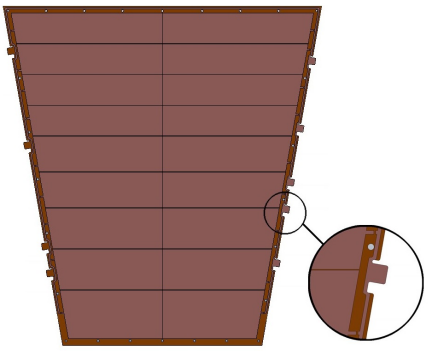

Figure 2.2: Layout of the GEM foil for the IROC prototype with a zoom on the HV-flap.

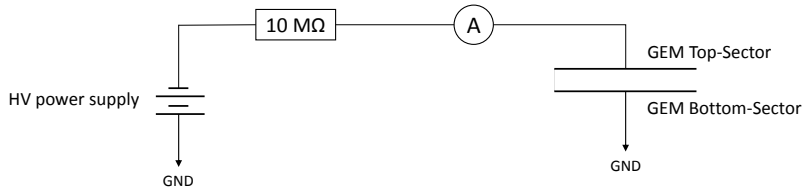

Figure 2.3: Powering scheme of the HV-tests.

HV-tests HV-tests of the foils are done at each step of the detector assembly to ensure proper and safe operation. Furthermore, these tests serve as a quality assurance step for new foils. The tests are conducted in a box flushed with nitrogen to ensure dry-gas environment and to prevent the foils from being damaged by sporadically occurring discharges. The potential difference applied between the GEM electrodes is increased in steps up to 600 V. The leakage current and the discharge rate are measured at each step of ramping. Figure 2.3 shows the powering scheme of the tests.

Frames The foils are glued on 2 mm fiberglass (G10) frames. The frames contain a 400 µm thick spacer grid to prevent the foils from approaching each other due to electrostatic forces. Before gluing, the frames are polished with fine sand-paper, cleaned in an ultrasonic bath and finally dried in the oven at 60°C for at least 8 hours.

Gluing Before gluing, the foil is stretched with a tension of ∼10 N/cm using a pneumatic stretching tool. A gluing robot dispenses the epoxy ARALDITE 2011 on the top side of the frame that is afterwards fitted into an alignment tool. With the help of Teflon pins, the stretched foil is aligned to the frame and finally glued. To assure proper contact between the foil and the frame, a heavy aluminium plate is put onto the foil without touching the active area and the glue is cured at 60°C for at least 24 hours. Then the raw material of the foil is cut off.

2.2 IROC alubody

The IROC alubody holds the pad plane and the triple GEM-stack and allows connection to the Front End Electronics [1].

Preparations for mounting Another HV-test is done with the framed foils. Afterwards, SMD loading resistors are soldered to the single sectors connecting them to

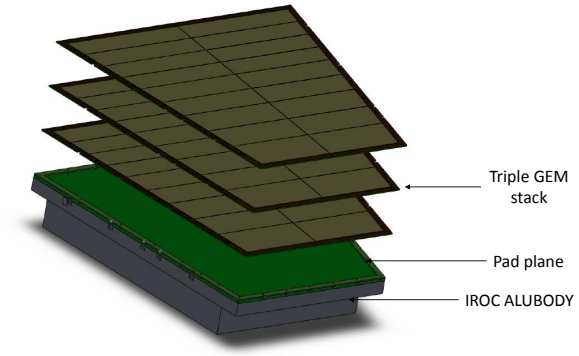

Figure 2.4: Exploded view of the mounted IROC prototype.

the main HV path of the GEM. The used resistors are the following:

- 10 MΩ for top (GEM1) and middle (GEM2) foils
- 1 MΩ for bottom (GEM3) foil.

Mounting The framed foils are one after the other mounted in a stack on the IROC alubody. The transfer and induction gaps are 2 mm, given by the thickness of the frames. Fiberglass M3 screws are used to fix the foils to the alubody. Kapton wires are soldered to the flaps to ensure HV connection. Figure 2.4 shows an exploded view of the IROC triple GEM-stack.

Connection to the pad plane In total, 5504 pads are integrated into the pad plane [1]. Connection to the pads is possible via 258 connectors mounted on the back side of the IROC alubody. For the measurements described in this work, analog summation cards were used to merge three connectors into one readout channel. Thus, 86 readout channels are available with the current set-up.

2.3 Test box

Once mounted, the IROC is transferred to the aluminium test box with a field cage (see Figure 2.5). The GEM-stack is fixed to the top side of the test box, which is basically a small drift chamber with a drift length of 10.6 cm. During this experiment, a drift field of 360 V/cm was used.

The test box has cut-outs with aluminized Mylar windows (50 µm) providing access for radioactive sources or beams from two sides of the box and from the bottom side.

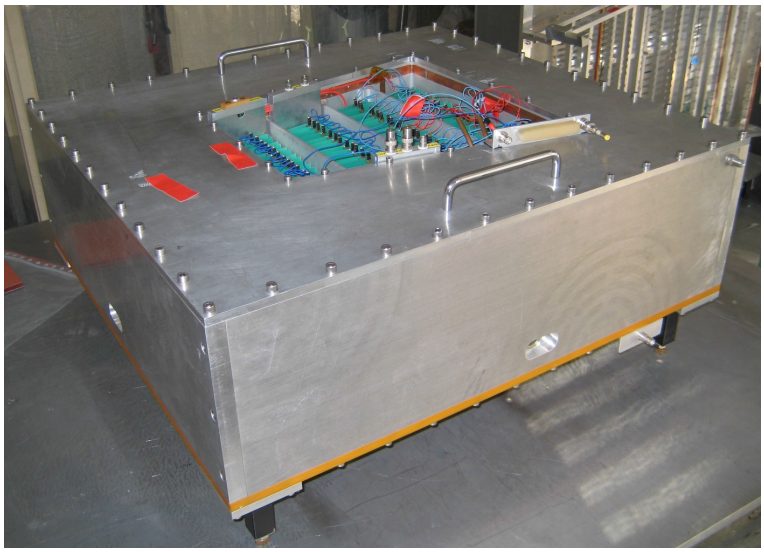

Figure 2.5: Picture of the IROC mounted to the test box.

Table 2.1 lists all materials built into the detector that will be in the beam line and thus absorbing energy.

Function	**Material**	**Thickness**
Detector window	Aluminized Mylar	50µm
Detector gas	Ne/CO_2	5cm
Fieldstrip	Aluminzed Mylar	25µm
Active Volume	Ne/CO_2	63.5cm
Fieldstrip	Aluminzed Mylar	25µm
Detector gas	Ne/CO_2	5cm
Detector Window	Aluminized Mylar	50µm

Table 2.1: Different materials in the detector.

Chapter 3

Preparations for the experiment at MLL

This chapter describes the preparations for the test beam at MLL. A simulation was conducted, furthermore rate calculations were done to optimize the setup and to choose proper beam settings and readout electronics for our purposes.

3.1 Mayer-Leibniz-Laboratorium

The experiment was conducted at the tandem accelerator of the Maier-Leibnitz-Laboratorium (MLL) [23] in Garching. The accelerator is a tandem Van-de-Graaf accelerator [24] with a maximum terminal voltage of 12.5 MV.

A stripper foil in the middle of the accelerator removes some of the outer electrons of the accelerated ion. This changes the polarity of the ion, such that it can be re-accelerated in the second part of the Tandem accelerator. For hydrogen ions, this implies that the maximal kinetic energy is $2{\cdot}12.5\,\mathrm{MeV} = 25\,\mathrm{MeV}$. Due to beam stability, the minimal beam energy is limited to around 10 MeV.

The maximal proton beam current can reach up to 1 µA ($\sim 1 \times 10^{12}$ Hz). In the experimental hall, where the experiment was set up (Hall II), the maximal beam current is limited to 10 nA ($\sim 1 \times 10^{10}$ Hz) due to radiation protection purposes.

For the purposes of this experiment, the ability to distinguish between beam-correlated discharges and uncorrelated discharges is crucial. In order to get a clear separation between these two cases a chopped beam was chosen. In general, the chopping of the beam is only limited by the beam stability. A stable operation can be achieved with pulses longer than ∼100 ns and a repetition rate between ∼250 Hz and ∼10 MHz.

3.2 Setup

The experiment was conducted at MLL in Hall II at $-10°$ beam line. The detector was placed directly after the beam pipe. On the exit aperture of the beam pipe a 50 µm Kapton window was mounted. The detector was positioned as close as possible to the exit window to reduce energy loss and scattering of the protons in the air gap (∼5 cm).

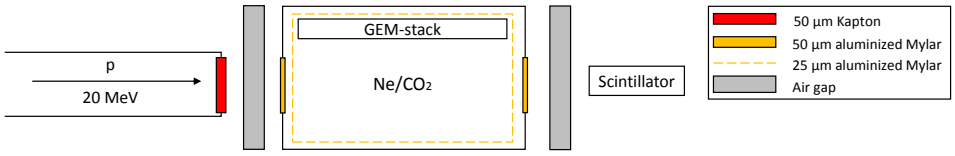

Figure 3.1: Sketch of the setup of the MLL experiment.

Due to a fault in the etching process, sector 5 of the second GEM in the stack used in this experiment had to be disconnected. Consequently, the box was positioned in such way, that the beam entered the box with a slight offset to shoot into the even numbered sectors. Figure 3.2 shows a top view of the positioning of the GEM sectors relative to the beam. Behind the test box a plastic scintillator was mounted for triggering (see Section 3.7). Figure 3.1 shows a sketch of the setup and indicates all materials that are directly in the beam line and thus absorbing energy of the protons.

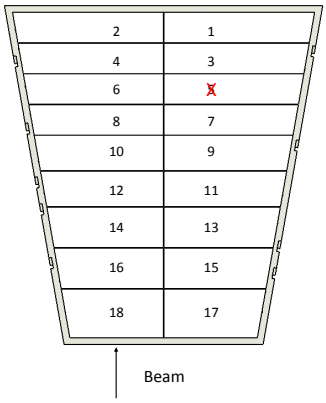

Figure 3.2: Top view of the positioning of the GEM sectors with the broken sector 5 crossed out.

3.3 Simulation

A simulation was conducted with the LISE++ software [25] to check the feasibility of the experiment and to choose right beam parameters for the measurement. The beam parameters were varied for the settings mentioned in Section 3.1. All materials mentioned in Table 2.1 with the additional Kapton window and the air gap were taken into account.

3.3.1 Energy deposition

The most important quantity of the experiment is the energy deposited by low-energy protons in the active volume of the detector, directly over the triple GEM-stack.

Particles in medium loose their energy mostly due to inelastic collisions with the electrons of the atoms in the material and elastic scattering on the nuclei, whereas the second point can be neglected compared to the first one. The formula for the calculation of the energy loss of a charge particle when traversing matter was established by Bethe [26]:

$$-\left\langle \frac{\mathrm{d}E}{\mathrm{d}x} \right\rangle = 2\pi N_a r_\mathrm{e}^2 m_e c^2 \rho \frac{Z}{A} \frac{z^2}{\beta^2} \left[\ln\left(\frac{2m_\mathrm{e}\gamma^2 v^2 W_\mathrm{max}}{I^2} \right) - 2\beta^2 \right], \tag{3.1}$$

where:

r_e	classical electron radius	ρ	density of the absorbing material
m_e	electron mass	z	charge of incident particle in units of e
N_a	Avogadro's number	β	$= v/c$ of the incident particle
I	mean excitation potential	γ	$= 1/\sqrt{1-\beta^2}$
Z	atomic number of the absorbing material	W_{max}	maximum energy transfer in a single collision.
A	atomic weight of the absorbing material		

This formula is the basis for all further calculations and simulations, as used for example by LISE++.

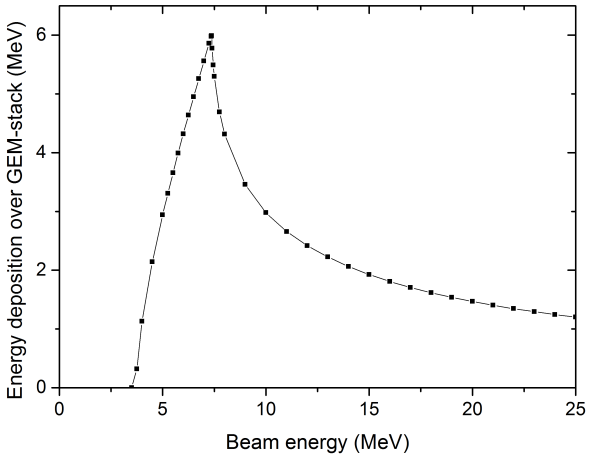

Figure 3.3: Energy loss of protons in the detector gas (Ne/CO_2) over the whole GEM-stack as a function of beam energy.

Figure 3.3 shows the energy deposited over the GEM-stack as a function of the beam energy. Up to 6 MeV are deposited over the detector by protons with a kinetic energy of 7.4 MeV, which is also the threshold energy for protons to pass through the entire test box and exit the detector. Protons with lower energy are stopped in the active volume and deposit there their full energy. Protons with higher energy are able to pass through the detector and will leave less energy in the active volume. It is then clear, that for the protons with an energy lower than 7.4 MeV the Bragg peak occurs within the active volume of the detector. Thus, a large part of the proton's energy is deposited in one spot. This implies a inhomogeneous irradiation of the chamber and thus the energy deposition over single sectors will vary a lot. In order to get comparable results for different sectors, a constant irradiation was chosen and thus a beam energy of 20 MeV. It is assumed, that all energy is deposited in the row with the even-numbered sectors due to the offset. The energy deposition over a single GEM sector is then rather constant, on the average around 120 keV (compare Table 3.1).

3.3.2 Energy and energy loss straggling

The previous section describes the results obtained for the simulation of the *mean* energy loss. However, the energy loss is a statistical process and thus even an initially monoenergetic beam will show a distribution in energy after having passed through matter. For thick absorbers, with a sufficient high number of collisions N of the traversing particle, the energy distribution will approach the Gaussian form

$$f(x, \Delta) \propto \exp\left(\frac{-(\Delta E - \langle \Delta E \rangle)}{2\sigma^2}\right), \tag{3.2}$$

where:

x	thickness of the absorber
ΔE	energy loss in the absorber
$\langle \Delta E \rangle$	mean energy loss in the absorber
σ	standard deviation.

Figure 3.4 shows the width σ of the energy distribution of the protons at the end of the GEM-stack depending on the beam energy. Clearly visible is the decrease of the distribution width with the beam energy, which was another reason to choose the 20 MeV beam energy.

As a starting point for the calculation of the energy loss straggling per GEM sector, the results of the energy straggling of the beam were taken. Then the energy loss over each sector was calculated within the values of the σ of the energy distribution, which gives the straggling of the energy loss as shown in Table 3.1. The energy loss straggling reaches up to 20 % of the energy deposited in one sector.

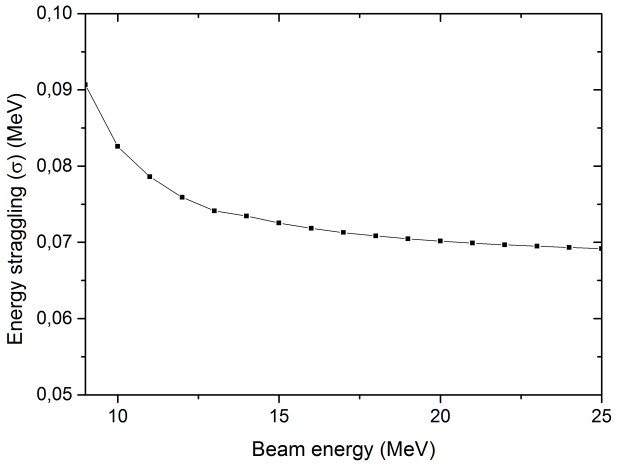

Figure 3.4: Width of the energy distribution of the proton beam in the detector gas (Ne/CO_2) at the end of the GEM-stack as a function of its energy.

GEM-Sector	Δ**E** (keV)	σ (keV)
2	102.22	17.692
4	105.76	17.956
6	105.26	17.964
8	104.74	18.104
10	121.59	19.551
12	120.90	19.540
14	137.34	20.865
16	136.45	21.059
18	156.51	22.513

Table 3.1: Energy loss and energy loss straggling for all GEM-sectors.

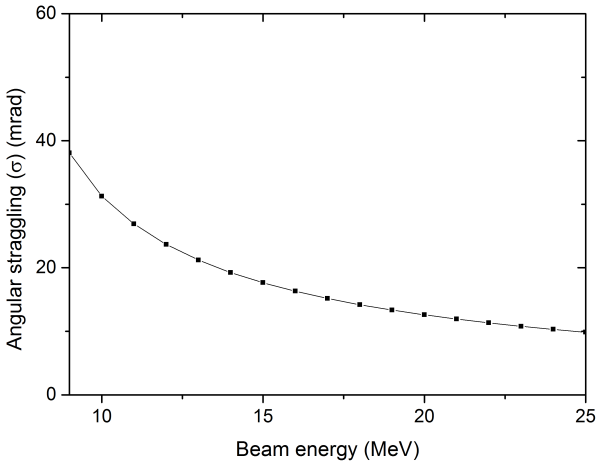

Figure 3.5: Width of the angular distribution of the beam in the detector gas (Ne/CO_2) at the end of the GEM-stack as a function of its energy.

3.3.3 Angular straggling

Each single collision of the incoming protons with the nuclei or electrons of the detector gas atoms or any other material deflects them in some way. As the energy distribution, also the angular distribution approaches to the Gaussian form with high enough number N of such collisions. The Gaussian distribution is centred around 0°. Figure 3.5 shows the σ of this distribution depending on the beam energy. For 20 MeV protons, the σ of the distribution is 12.6 mrad which is smaller than 1°.

This rather low value assures that, on the average, all protons will be able to traverse the test box and reach the scintillator.

3.4 Rate calculations

3.4.1 Charge over one GEM-sector

The results of the simulations described in Section 3.3.1 show that 20 MeV protons deposit maximally around (160 ± 20) keV in the detector gas over one GEM-sector. The effective ionization potential of the detector gas Ne/CO_2 is W_i=38.097 eV [27]. Thus, one single proton will produce around (4100 ± 600) primary electrons. With an assumed gain in the GEM-stack of 1000, the electron cloud drifting to the pad

plane and inducing a signal there will carry a charge of $(0.66 \pm 0.09)\,\mathrm{pC}$ per single proton depositing energy over the GEM-sector.

3.4.2 Choosing the beam parameters

The idea of this experiment was to approach the expected current of the last GEM-foil in the ALICE TPC in order to reproduce the conditions there. The current expected on one single sectors of the last GEM-foil in the ALICE TPC after the LS2 is 250 nA [27]. Under the assumption that this is a constant current, the equivalent rate for 20 MeV protons can be calculated as

$$\frac{1}{t} = \frac{I}{Q} = 379\,\mathrm{kHz}. \tag{3.3}$$

In order to get a clear separation between beam correlated and uncorrelated discharges, a chopped beam was chosen. The spill length was set to 500 ns and the interval between two spills was 20 µs (50 kHz).

With these information, the beam current necessary to reproduce the conditions at ALICE is

$$I = \frac{Q}{t} = \frac{379\,\mathrm{kHz} \cdot 1.6 \times 10^{-19}\,\mathrm{C}}{50\,\mathrm{kHz} \cdot 500\,\mathrm{ns}} = 2.43\,\mathrm{pA}. \tag{3.4}$$

As a starting point for the experiment a beam current of 1 pA is defined. The current is to be increased until the value expected at ALICE is reached. If the chamber is stable at this stage of the experiment, the beam current and thus the current on the GEMs is to be increased until the stability is strongly affected.

3.4.3 Expected signals

In order to get a rough estimation if the signals of a discharge can be distinguished from usual signals by protons, both are calculated.

Each single pad of the pad plane has its own specific capacitance of below 9 pF as mentioned in [1]. In total the IROC pad plane has 5504 pads. Under the assumption that the pads are distributed equally, the area on the pad plane under one GEM-sector consists of ∼306 pads. To get the capacitance of the area on the pad plane under one GEM-sector, the capacitances of single pads are summed up

$$C_{\mathrm{channel}} = \sum_{i=1}^{n} C_{i,\mathrm{pad}} = 2.75\,\mathrm{nF}. \tag{3.5}$$

The electron avalanche produced by a single proton carries a charge of 0.66 pC at

Discharge	**Expected charge in a discharge** (μC)	
	Standard settings	IBF settings
GEM1	2.50	1.13
GEM2	1.83	1.18
GEM3	1.60	1.43
From GEM 3 to Pad plane	0.60	0.61

Table 3.2: Expected charge in a discharge.

a gain of 1000. With the pad plane in principle being a capacitor, the signal that the electron avalanche induces on the pad plane can be calculated as

$$V = \frac{Q}{C_{\text{channel}}} = 0.24\,\text{mV}. \tag{3.6}$$

In order to find out if this signal can be distinguished from the signal of a discharge, the latter is calculated. Under the assumption, that the whole charge stored in one sector of a GEM-foil is freed during a discharge, this charge can then be calculated via

$$Q_{\text{discharge}} = C_{\text{GEM}-\text{sector}} \cdot \Delta V_{\text{GEM}}, \tag{3.7}$$

with the capacitance of a GEM-sector of 5 nF and the potential difference from Tables 1.1 and 1.2.

For the calculation of the charge freed during a discharge propagating from the bottom side of GEM3 to the pad plane, it is assumed that the discharge contains 100% of the charge between the bottom side of GEM3 and the padplane [28]. This charge is then

$$Q_{\text{discharge}} = C_{\text{GEM3}-\text{pad plane}} \cdot \Delta V_{\text{GEM}}, \tag{3.8}$$

where the capacitance $C_{\text{GEM3}-\text{pad plane}}$ between the bottom side of GEM3 and the pad plane is 800 pF and ΔV the potential difference between GEM3 and the pad plane. The results are shown in Table 3.2.

Although this calculations are based on rough assumptions and simplifications, the charge freed during a discharge will be several orders of magnitude higher than the charge of a usual proton signal. Thus, a discharge can easily be distinguished from the signal produced by single protons.

3.5 Readout scheme

Due to the fact, that the mentioned PCB cards (compare Subsection 2.3) sum up three pad sectors each, the readout sectors could not be chosen in such way, that one readout sector covers the area of only one GEM-sector. Thus the pad plane was divided into eight independent readout sectors covering the area of approximately two GEM-sectors each. Figure 3.6 shows the result of this division.

The prerequisites for the readout are to

- store the raw signal,
- measure the pulse height of the signals,
- count discharges and correlate them with the presence of the beam.

The raw signal is processed with an oscilloscope, the pulse height is stored to disk with an ADC and a scaler counts the discharges. To trigger the ADC and the scalers, the signal of the scintillator is converted into a gate. Passive, resistive signal splitters [5] are used to supply all different readout branches with the raw signal. Figure 3.7 shows the scheme of the readout chain of the experiment. The following subsections introduce the different branches of the readout of this experiment.

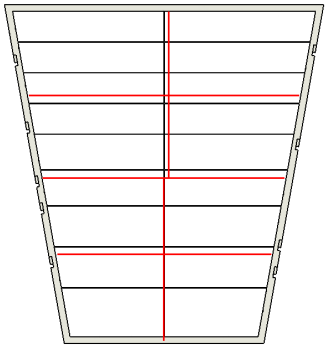

Figure 3.6: GEM-segmentation (*black*) compared to readout sector division (*red*).

3.5.1 Scintillator-branch

The signal from the scintillator is converted into a gate to trigger the ADC and the scaler.

The scintillator branch consists of a scintillator, a photomultiplier pre-amp, a discriminator and a gate generator. The scintillator is a common plastic scintillator with an integrated photomultiplier tube. The threshold of the LeCroy 620D discriminator is set high enough not to trigger on noise. To trigger all other branches, a gate generator is used. The gate width is adjusted to the drift time of the primary electrons ($\sim$4 µs) to synchronize the opening of the gate with the signal induced on the pad plane.

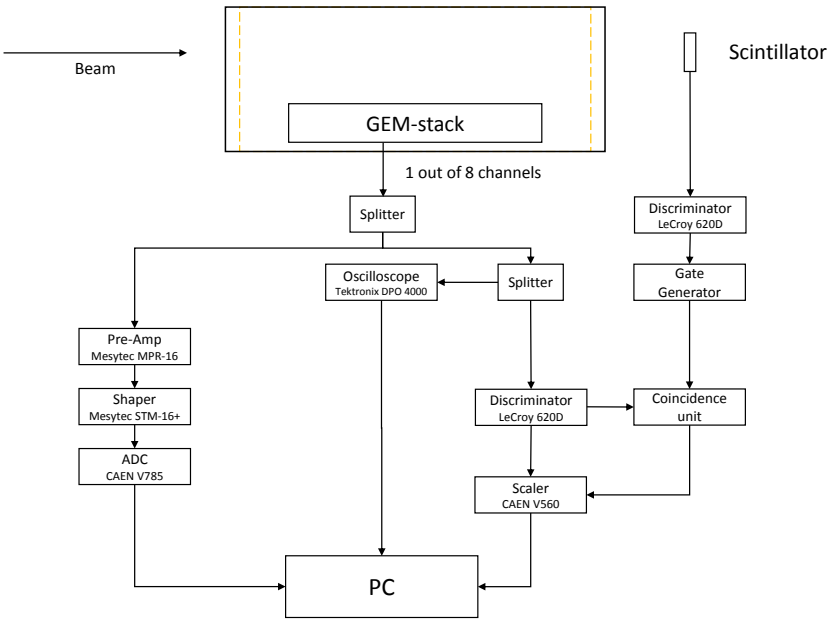

Figure 3.7: Scheme of the readout used for the MLL beamtime.

3.5.2 ADC-branch

This part of the readout is inherited from the SiΛVio detector developed in the Kaon Cluster Group [29]. It consists of a Mesytec MPR-16LOG logarithmic pre-amplifier, a Mesytec STM-16+ shaper and a CAEN V785 peak-sensing ADC. The ADC is read out via the VME backplane.

The pre-amplifier is designed for the readout of Silicon detectors. At an energy range of 10 MeV [30], it changes its scale from linear to logarithmic. To convert this energy range in Silicon into an equivalent charge carried by the electron cloud onto the pad plane, the energy range is divided by the band gap energy of Silicon (3.6 eV) and multiplied with the elementary charge e.

$$Q = \frac{10\,\mathrm{MeV}}{3.6\,\mathrm{eV}} \cdot 1.6 \times 10^{-19}\,\mathrm{C} = 0.44\,\mathrm{pC}. \tag{3.9}$$

Thus, if the charge, that induces the signal on the pad plane, exceeds 0.44 pC, the pre-amplifier changes from linear to logarithmic scaling. The maximal energy range of the pre-amplifier is 3 GeV, which is equivalent to a charge of 133 pC.

3.5.3 Scaler-branch

As shown above, the signal of a discharge is supposed to massively exceed the signal expected from single protons. This is the basic idea of the scaler branch to count the discharges.

It consists of a LeCroy 620D discriminator set to the highest possible threshold of 1 V, which is equivalent to a charge inducing the signal on the pad plane of $\sim$6.2 nC. This threshold voltage will be exceeded by the signal of a discharge but not by a normal signal. This ensures that the discriminator only gives a logic signal when there was a discharge in one of the GEM-sectors over the readout sector. After the discriminator, the logic signal goes into two branches (see Fig. 3.7): one part is directly connected to a scaler to count all discharges, whereas the other part goes to a coincidence unit receiving a common inhibit from the scintillator gate as long as a signal from protons is expected (beam off discharges). Then this signal goes to the scaler as well. This allows to count the beam correlated and uncorrelated discharges. The scaler is read out via the VME backplane.

3.5.4 Oscilloscope

The raw signal is read out with a TEKTRONIX DOP 4000 oscilloscope connected via Ethernet to a PC with a LabView program for remote control.

Chapter 4

Results and discussion

This chapter shows the results of all measurements performed during this thesis including the beamtime at MLL.

4.1 Gain measurements

The IROC test box was flushed with two different detector gases (Ne/CO_2 and Ar/CO_2 in the ratio 90/10 each). A Fe-55 source was mounted to the Mylar window on the bottom side of the box. Fe-55 is a γ-source that emits low-energy photons with a mean energy of $E_\gamma = 5890\,\mathrm{keV}$. These photons ionize the detector gas and thus produce primary electrons drifting to the GEM-stack. After amplification, they are collected on the pad plane, thus the anode current may be measured with an amperemeter. Spectra were taken with an Amptek Multichannel Analyzer MCA8000A for rate and energy resolution measurements. The current on the pad plane was measured with pico-amperemeters developed at TUM E18. Measurements were performed for different HV-settings, scaling factors and gas mixtures.

The gain strongly relies on the density of the detector gas and thus on several parameters like for example ambient pressure and temperature. Thus, in order to obtain comparable results, the gain curves should be corrected for these parameters. No p/T-corrections were applied to the gain curves obtained during this thesis.

Figures 4.1 and 4.2 show the spectra taken with the MCA. The large peak in both spectra is due to the full absorption of a Fe-55 γ.

The small peak in the Ar/CO_2 spectrum (Fig. 4.2) around ADC channel 300 is a so-called escape peak. If the energy of the incoming γ is larger than the absorption edge of the detector gas, the gas atoms can get excited. A characteristic γ of the gas is produced and thus the energy of the incoming γ decreased by the excitation energy. Consequently, the escape peak is shifted by the excitation energy towards lower energies. For Ar atoms this implies that the peak is shifted by 3.2 keV.

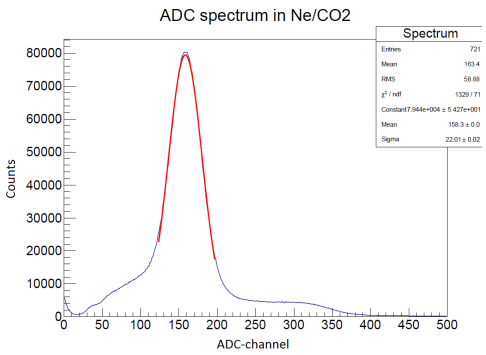

Figure 4.1: ADC spectrum of the Fe-55 source in Ne/CO_2 at 73% HV-scaling factor.

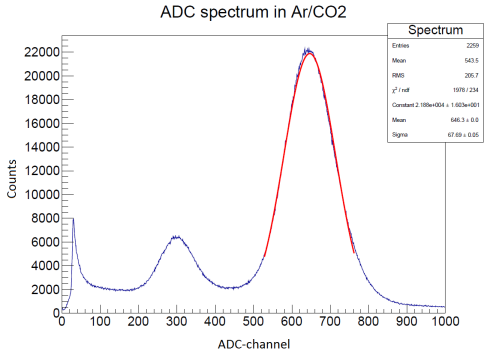

Figure 4.2: ADC spectrum of the Fe-55 source in Ar/CO_2 at 87% HV-scaling factor.

4.1.1 Gain measurements

The ratio between the current on the anode and the calculated current of the primary electrons produced by the γ-source is defined as effective gain.

$$G = \frac{I_{\text{meas}}}{I_{\text{source}}} = \frac{I_{\text{meas}}}{E_\gamma / W_i \cdot e \cdot \phi}, \tag{4.1}$$

where:

W_i	effective ionization potential of the gas mixture
e	the elementary charge
ϕ	the rate of the source.

The total gain uncertainty is determined by the standard deviation of the rate measurement and the uncertainty given by the current meter.

The gain measurements were performed for two different HV-settings. The standard setting was measured in Ne/CO_2 and Ar/CO_2 whereas the IBF setting was only measured in Ne/CO_2. The scaling factors were varied for the standard settings in Ne/CO_2 from 59% - 73% and in Ar/CO_2 from 81% - 87%. For the IBF setting in Ne/CO_2 the scaling factors were varied from 95% - 100%.

The results are shown in Figures 4.3, 4.4 and 4.5. One can observe, that the gain is much lower for the IBF settings than it is for the standard settings. The comparison between the two used detector gases shows, that in Ne/CO_2, the same gain can be achieved with lower electric fields than in Ar/CO_2.

For lower gas gains, the signals are so small, that the peak is already at the edge of what the MCA can process. Even though the signals were pre-amplified, the quality of the spectra was rather poor, especially for the IBF settings. This is the reason for the rather large errors in Figure 4.5.

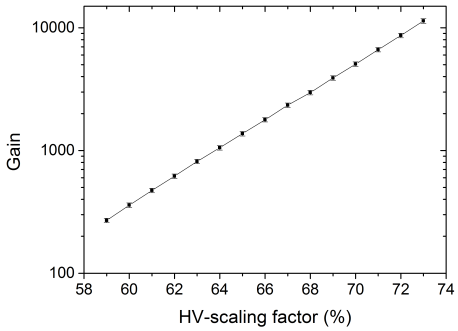

Figure 4.3: Gain in Ne/CO_2 with standard HV-setting.

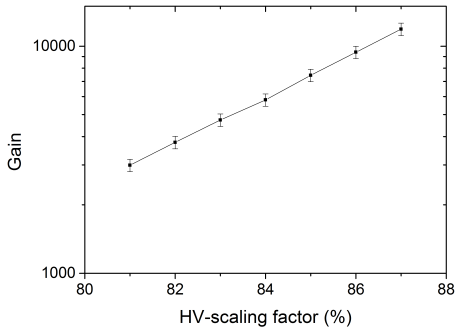

Figure 4.4: Gain in Ar/CO_2 with standard HV-setting.

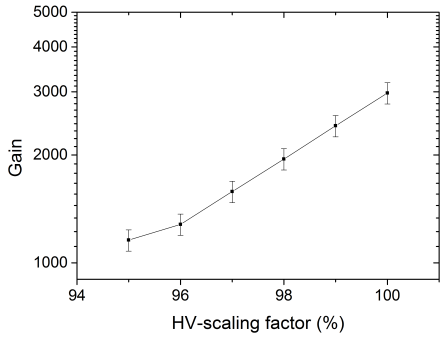

Figure 4.5: Gain in Ne/CO_2 with IBF HV-setting.

4.1.2 Energy resolution

The energy resolution was extracted from the spectra taken with the MCA. The peak in the spectrum was fitted with a Gaussian and the centroid of the peak μ with its width σ was calculated. In order to reduce the contribution of noise to the final result, a polynomial or exponential function was fitted to the background. The relative energy resolution is then

$$\frac{\sigma}{\mu}. \tag{4.2}$$

The energy resolution was calculated for different HV-settings and scaling factors. The scaling factors were varied for the standard settings in Ne/CO_2 from 69% - 73% and in Ar/CO_2 from 81% - 87%. For the IBF setting in Ne/CO_2 the scaling factors were varied from 95% - 100%.

The large fluctuations are due to the already mentioned problems with the quality of the spectra. Furthermore, systematic error sources in this setup are under investigation.

Figures 4.6, 4.7 and 4.8 show the energy resolution versus the HV scaling factor. Despite the fluctuations, the tendency is clearly observable. Noticeable is the rise of the energy resolution with the gain in Figure 4.8. Further investigations are ongoing, if this is related to the field configuration of the IBF settings.

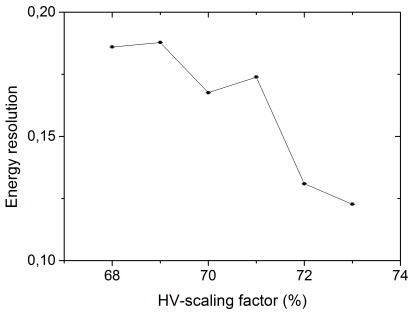

Figure 4.6: Energy resolution in Ne/CO_2 with standard HV-setting.

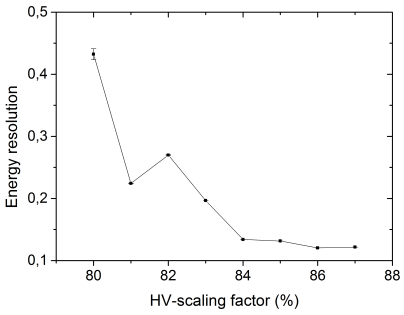

Figure 4.7: Energy resolution in Ar/CO_2 with standard HV-setting.

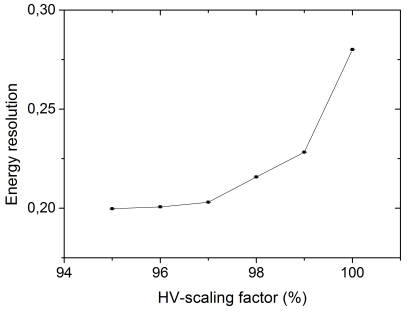

Figure 4.8: Energy resolution in Ne/CO_2 with IBF HV-setting.

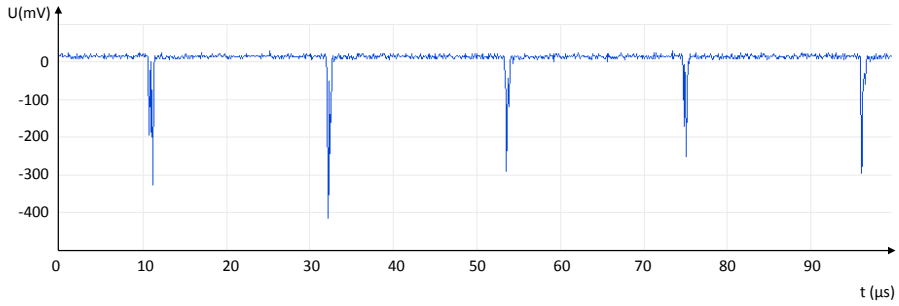

Figure 4.9: Structure of the beam measured with the scintillator.

4.2 Analysis of the measurements at MLL

This section focuses on the analysis of the data taken at MLL during the test beam in July 2013 stressing the results of the ADC-spectra and HV-supply trips.

4.2.1 The beam

Due to the chopping, the beam current was very unstable. This resulted in a special structure of the beam with a varying number of protons per spill, in-between one and ∼10. Figure 4.9 shows a plot of the scintillator signals over a larger time-scale of 100 µs. The signals of single protons can be observed, but also pile-ups of several protons.

The measurements mentioned in this section were performed with a beam current of 20 nA at the source. When the beam was chopped, the current was varying between 1.4 - 2.5 nA.

Later during the experiment, the source current was increased to 65 nA, resulting in a chopped current of 4.5 - 8.1 nA.

Figure 4.10 shows the current on the HV-divider that supplies the GEM-stack. One can see, that the current sharply rises when the beam is turned on. Also fluctuations in the GEM current of the order of ∼5 µA can be observed, which are due to the mentioned pile-up. For higher gas gains, these high spikes were exceeding 25 µA.

4.2.2 Raw signals

Raw signals were taken for the standard HV-settings at 60%. One example can be seen in Figure 4.11.

In the upper part of the picture the signal of the scintillator and the shaper signal can be seen. The delay between both of them is around 2.5 µs. This delay is due to

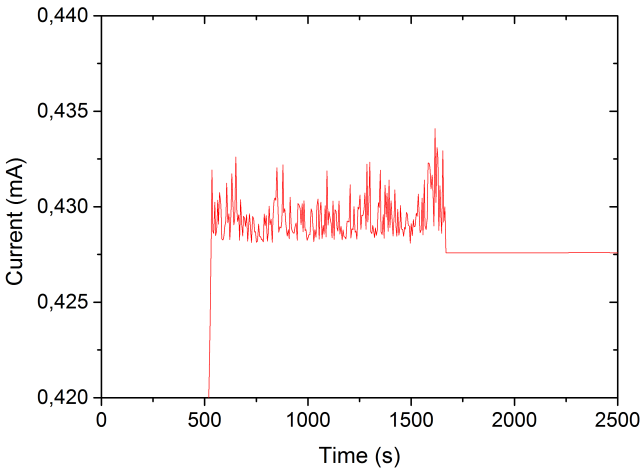

Figure 4.10: Current on GEM HV-divider with beam on and beam off.

Figure 4.11: Signal taken with the oscilloscope. The upper part shows the signal of the scintillator (*white*) and the shaper signal (*red*). The lower part shows the actual raw signal.

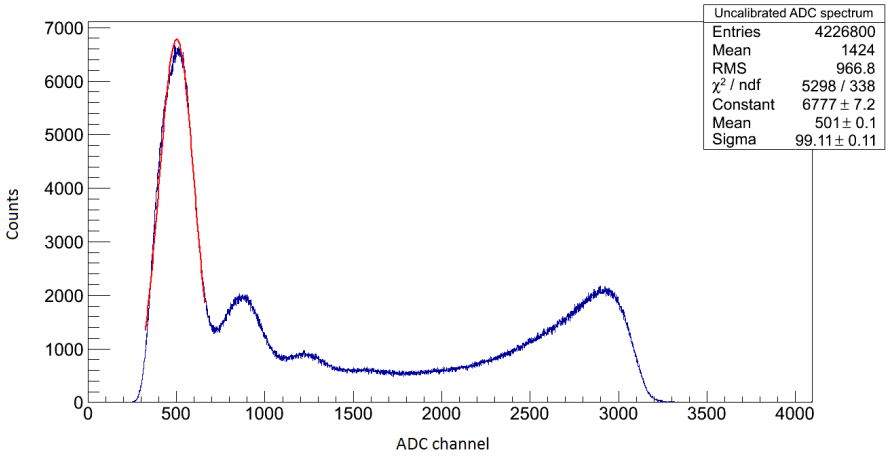

Figure 4.12: Uncalibrated ADC spectrum for 60% HV-scaling factor with a Gaussian fitted to the single proton peak.

the drift time. In the lower part of the figure, on can see the raw signal induced on the pad plane. This signal is barely visible and hidden in the noise, which could be due to the low gain and the long cables to the oscilloscope.

4.2.3 ADC-spectra

Data was taken half hour each for the standard HV-setting for scaling factors 60-66% and 69%, which corresponds to a gain range of 350–3000.

All data shown here were taken from the channel that reads out the part of the pad plane covering the area of sectors 12 and 14.

Figure 4.12 shows an uncalibrated ADC spectrum. One can observe a structure with several peaks. The first peak is associated to a single proton in one spill depositing its energy in the chamber. The second peak is probably due to a pile-up of two protons per spill, the third due to three protons per spill and the barely visible forth peak due to four protons in one spill. The rise towards ADC channel ∼3000 is probably due to 5-10 protons per spill. The peaks are merged together due to the logarithmic scaling of the pre-amplifier.

Appendix A shows the histograms. For higher HV scaling factors, one can observe that the single and double proton peaks slowly merge into a washed out single-peak-structure.

Contrary to all other spectra, the spectrum of the HV scaling factor 69% looks different: The rise towards the first peak is rather long (∼1000 ADC channels) and the peak itself is much broader than in the other spectra. Additionally, this is the

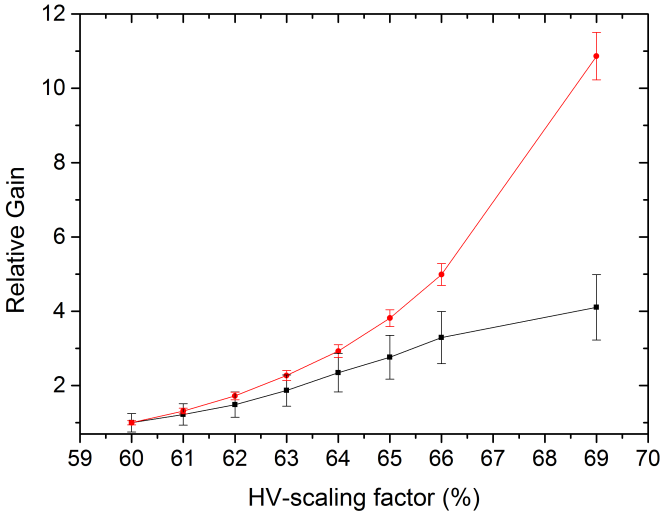

Figure 4.13: Relative gain drawn from the ADC spectra (*black*) compared to the gain measured in Section 4.1.1 (*red*).

only spectrum, where the 5-10 proton peak is not cut around ADC channel 3500. Due to the fact, that ADC spectra for 67% and 68% are missing, it is hard to say, if this behaviour is expected or that the boundary conditions of the experiment changed and thus this spectrum cannot be compared to the other ones.

4.2.3.1 Relative gain measurement

In order to test if the first peak visible in each of the histograms can be really assigned to the charge deposited by a single proton, the relative gain is extracted. A Gaussian is fitted to the peak in the histogram for each HV-setting. The mean ADC channel μ of the Gaussian of the single-proton peak is normalized to the peak at 60%. The relative gain g is then

$$g_i = \frac{\mu_i}{\mu_{60\%}}. \tag{4.3}$$

Also the gain measured in Section 4.1.1 is normalized to 60%. The result is shown in Fig. 4.13.

Although the tendency is the same for both measurements, a systematic shift can be observed between the two measurements. Especially for 69%, the difference is

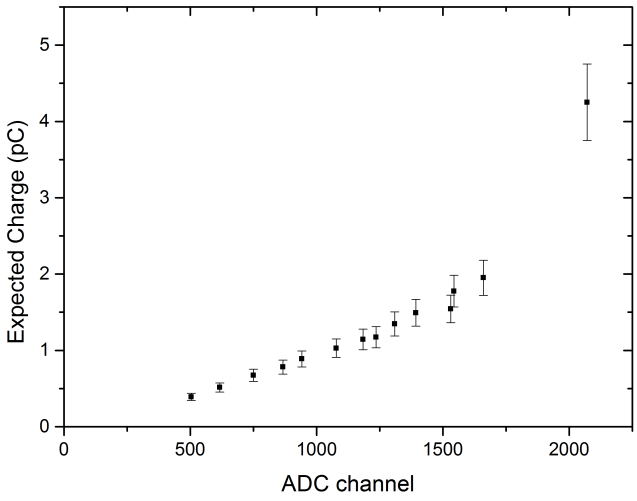

Figure 4.14: Mean ADC channel versus expected charge.

rather large (factor of ∼3). But as mentioned above, the spectrum of 69% is so far not completely understood and further examinations are ongoing.

One possible explanation for the observed difference between both measurements is the already mentioned p/T-dependency of the gain. The measurements were done completely independent from each other at different places and days. Thus, it is highly likely, that the density of the gas and thus the gain changed in-between both measurements. Nevertheless it is very probable, that the high, first peak in the ADC spectrum can be assigned to single protons.

4.2.3.2 Calibration

The calibration of the ADC spectra relies on the comparison between measured ADC values with the corresponding charge values obtained in the simulation.

The energy deposition is (260 ± 30) keV for this readout sector. Thus, the number of primary electron is (6800 ± 800) which is scaled for different HV-settings and thus gains.

The mean ADC channel of the Gaussian of the single proton peak is compared to the charge expected. For the HV-scaling factors 60%, 61%, 62% and 63%, also the double proton peak was taken into account and for 60% and 61% even the triple proton peak. Figure 4.14 shows the result.

Although the begin of the logarithmic scaling is already expected above HV-setting

61% (∼0.52 pC deposited charge, ADC-channel ∼620), one can observe that the rise is perfectly linear except for the last point. An increase towards the logarithmic scale can be observed for the last point. It should be noted, that this point was taken from the questionable 69% spectrum.

Nevertheless, these observations contradict the above mentioned assumptions and calculations.

According to the specifications of the pre-amplifier [30], the end of the linear scaling corresponds approximately to ADC channel 2800 (see Appendix B), which fits to what can be observed in the spectra.

Under the assumption that the results obtained in the simulation are correct, one highly possible explanation for these observations is that the signal transmission from the pad plane to the ADC was not 100% efficient. Furthermore, the influence of the passive, resistive splitters is to be examined.

The specifications of the pre-amplifier and the shaper used in this experiment give a further hint: The rise time of the pre-amplifier is rather short (12 ns), whereas the decay time is rather long (10 µs). On the other hand, the shaping time of the shaper is 0.4 µs. Thus, a huge part of the signal was cut off before it went to the ADC.

Due to the above mentioned contradictions between the simulations and the measurements, it was impossible to do a proper calibration of the ADC readout branch.

4.2.4 HV supply trips

The mentioned discharges during the test beam campaign at CERN could be observed due to trips of the HV power supply.

An additional current will be drawn from the power supply during a discharge. If this current is detected by the power supply, it will shut down. Table 4.1 lists the currents expected during a discharge in the GEM-stack for both HV-settings.

During this test beam, the current limit of the power supply was varied between 5 and 100 µA.

Part of the GEM stack	**Expected current during a discharge** (µA)	
	Standard settings	IBF settings
GEM 1	3.17	2.11
GEM 2	2.65	2.30
GEM 3	15.23	23.50
From GEM 3 to Pad plane	144.87	245.96

Table 4.1: Expected current during a discharge throughout the GEM-stack [28].

Also the fluctuations of the beam mentioned in Subsection 4.2.1 are exceeding at least low current limits used during the experiment (spikes up to 25 µA). The

Beam	**Current limit** 5 µA	**Current limit** 10 µA
On	3	6
Off	0	0

Table 4.2: Trips standard setting.

Beam	**Current limit** 50 µA	**Current limit** 100 µA
On	1	5
Off	0	0

Table 4.3: Trips IBF setting.

comparison to the values listed in Table 4.1 shows, that single discharges do not trigger the power supply to trip. Thus, the trips were either due to a propagated discharge to the pad plane or caused by the fluctuations of the beam (for low current limits).

4.2.4.1 Standard settings

In total, the standard settings were running ∼24 h with beam on. The HV-scaling factor was varied between 60% and 69%. 9 trips were observed as shown in Table 4.2.

Due to the high fluctuations of the beam that were actually exceeding the current limits of the power supply used here, it is most probable, that all trips mentioned above were only due to the low current limit (compare Table 4.1). After the current limit was changed to 50 µA, no single trip was observed.

4.2.4.2 IBF settings

In total, the IBF settings were running ∼5 h with beam on. One trip was recorded when ramping up from 95% to 96% with the beam turned on. All 6 other trips occurred at 100% as shown in Table 4.3

The current limits were increased by a factor of 10 compared to the limits during the standard settings run. This makes sure, that the current limit is only exceeded by discharges and not due to fluctuations of the beam. Contrary to the previous subsection, one can clearly conclude from this data that all trips were due to discharges.

Moreover, the comparison with Table 4.1 shows, that only propagating discharges in fact exceed the current limit of the power supply. Thus, the observed trips might be correlated with propagating discharges to the pad plane.

Chapter 5

Conclusion

5.1 Summary

Stability is one of the most crucial issues for GEM-based detectors. This is the reason, why stability tests, as performed in this thesis, are very important to ensure proper operation of the future readout chambers.

The stability of a GEM-based gas detector in Ne/CO_2 has been tested for different HV-settings of the GEMs and beam currents. To simulate the influence of slow, highly ionizing particles on the stability, the IROC prototype has been tested with low-energy protons at MLL (Mayer-Leibniz-Laboratorium).

A setup dedicated to systematic stability studies has been planned, commissioned and tested.

Furthermore, the gain curve and energy resolution of a GEM-based detector has been measured for different HV-settings.

As shown in this thesis, the gain of the IBF settings at 100% is lower compared to the standard setting 69%. Thus even with a lower charge density in the GEM-holes, the IBF settings may be more problematic than the standard settings.

Concluding, one can say, that changing the HV-setting drastically decreases the stability of the chamber. The stability problems of the IBF settings are probably due to the highest amplification in the third GEM and additionally the high induction field may increase the discharge propagation probability. The experiment has shown, that the IBF settings may be problematic and that the discharge probability is higher for the IBF settings than it is for standard settings.

Although the statistics are rather low, one can already say that highly ionizing particles at low rates (50 kHz) can provoke discharges in a GEM-based gas detector.

Still, for final conclusions a systematic study of discharge probabilities is necessary.

5.2 Outlook

In order to obtain final conclusions, a dedicated test beam in October is planned to get more statistics to validate and endorse the results obtained in this thesis.

It is planned to have a more fluent transition between both types of settings to obtain more information about the influence of the HV-settings on the discharge probability. Furthermore, a measurement of all available HV-settings is planned. The correlation between discharges and trips will be examined. A proper calibration of the ADC-branch with an α-source injected to the detector gas is planned. Also a series of gain measurements for p/T correction is foreseen.

The next step in the investigation of stability issues in a GEM detector will be systematic studies concerning the discharge probability with different radiation sources.

A series of tests with smaller detectors is planned. The reduced size of these detectors allows a much faster change of parameters than it is at the moment feasible with the IROC and the test box.

Appendix A

ADC spectra

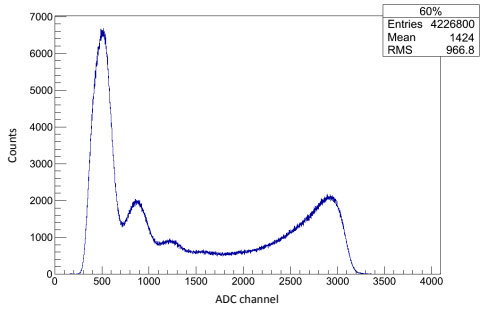

Figure A.1: ADC spectrum at 60% HV-scaling factor.

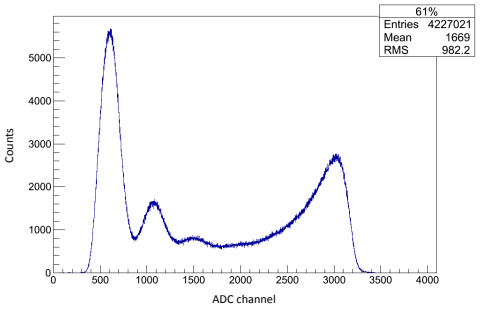

Figure A.2: ADC spectrum at 61% HV-scaling factor.

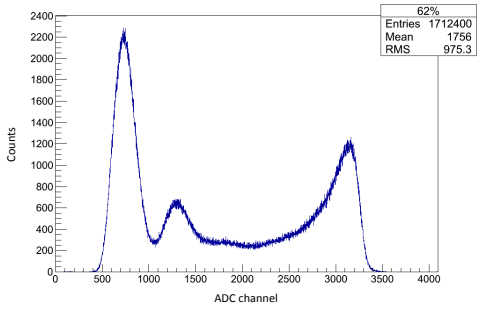

Figure A.3: ADC spectrum at 63% HV-scaling factor.

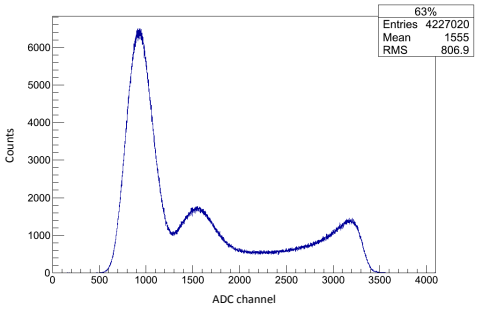

Figure A.4: ADC spectrum at 63% HV-scaling factor.

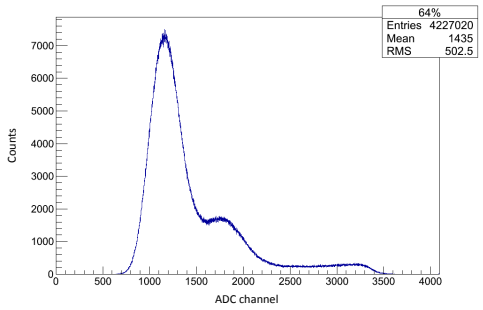

Figure A.5: ADC spectrum at 64% HV-scaling factor.

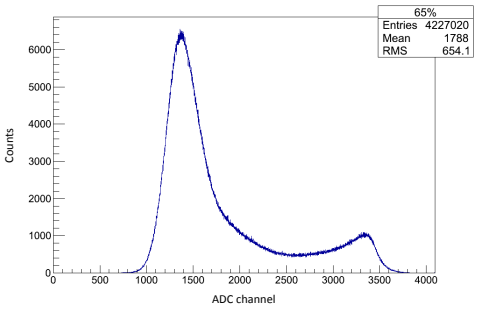

Figure A.6: ADC spectrum at 65% HV-scaling factor.

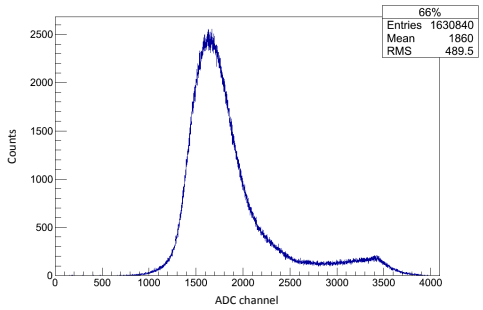

Figure A.7: ADC spectrum at 66% HV-scaling factor.

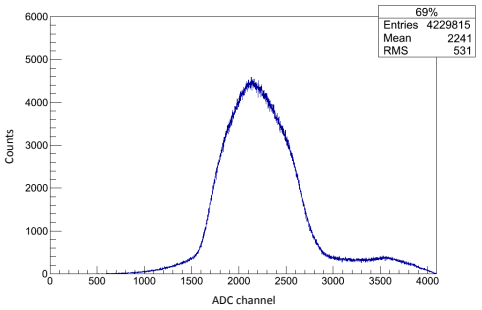

Figure A.8: ADC spectrum at 69% HV-scaling factor.

Appendix B

Pre-amplifier MPR-16LOG

This chapter shows the rough calculation of the ADC channel, where the begin of the logarithmic scale is expected.

Figure B.1 shows the output voltage of a Mesytec STM-16+ shaper as a function of the input energy of the pre-amplifier MPR-16LOG. 10 MeV correspond to a charge of 0.44 pC. One can see, that the logarithmic scale is expected to begin at an output voltage of the shaper of ∼5.5 V.

The maximal input voltage of the CAEN V785 ADC is 8 V [31]. Thus, the logarithmic range is expected to begin around ADC channel

$$\frac{V_{\text{Shaper output}}}{V_{\text{ADC input}}} \cdot 4096 = \frac{5.5\,\text{V}}{8\,\text{V}} \cdot 4096 = 2816, \tag{B.1}$$

which fits to what can be observed in the spectra.

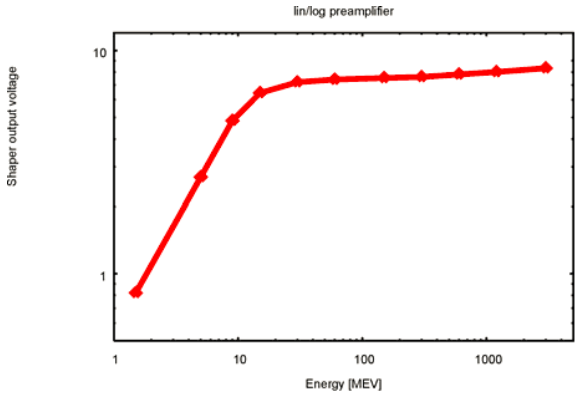

Figure B.1: Shaper output voltage as a function of input energy of the Mesytec MPR-16LOG pre-amplifier (from [30])

Bibliography

[1] ALICE Collaboration, Nucl. Instr. and Meth. A **622**, 316 (2010).

[2] D. R. Nygren and J. N. Marx, Phys. Today **31N10**, 46 (1978).

[3] M. Kotulla et al., *Technical Progress Report for PANDA: Strong Interaction Studies with Antiprotons* (2005).

[4] S. Afanasiev et al., Nucl. Instr. and Meth. A **430**, 210 (1999).

[5] W. R. Leo, *Techniques for Nuclear and Particle Physics Experiments*, Springer, Second Edtion (2009).

[6] G. Charpak et al., NIM **62**, 262 (1968).

[7] C. Garabatos, Nucl. Instr. and Meth. A **535**, 197 (2004).

[8] ALICE Collaboration, Journal of Instrumentation 3, S08002 (2008).

[9] F. Sauli, Nucl. Instr. and Meth. A **386**, 531 (1997).

[10] F. Sauli et al., Nucl. Instr. and Meth. A **560**, 269 (2006).

[11] L. Fabbietti et al., *Technical Design Study for the PANDA Time Projection Chamber* (2012).

[12] C. Altunbas et al., Nucl. Instr. and Meth. A **490**, 177 (2002).

[13] B.Ketzer et al., arXiv:1303.6694v1, *to be published* (2013).

[14] S. Blatt et al., Nucl. Phys. B (Proc. Suppl.) **150**, 155 (2006).

[15] F.V.Böhmer, Nucl. Instr. and Meth. A **719**, 101 (2013).

[16] A. Lebedev, Nucl. Instr. and Meth. A **478**, 163 (2002)

[17] V. Peskov and P. Fonte, *Research on discharges in micropattern and small gap gaseous detectors* (2009).

[18] H. Raether, *Electron avalanches and breakdown in gases*, Butterworths (1964)

[19] Yu. Ivaniouchenkov et al., Nucl. Instr. and Meth. A **422**, 300 (1999).

[20] P. Fonte et al., Nucl. Instr. and Meth. A **416**, 23 (1998).

[21] M. Ball, *Private communication.*

[22] S. Duarte Pinto et al., Journal of Instrumentation 4 (2009) P12009.

[23] Maier-Leibnitz-Laboratorium, http://www.bl.physik.uni-muenchen.de (16. June 2013).

[24] P.H. Rose and A.B. Wittaver, Sci. Am., **233**, 24 (1970).

[25] O.D. Tarasov and D. Bazin, Nucl. Instr. and Meth. B **266**, 4657 (2008).

[26] H. Bethe, Annalen der Physik, **397**, 325 (1930).

[27] C. Garabatos, *Private communication.*

[28] P. Gasik, *Private communication.*

[29] R. Münzer, *SiΛViO - Ein Trigger für Λ -Hyperonen*, Technische Universität München, Diplomarbeit (2008).

[30] Mesytec, http://www.mesytec.de/silicon.htm (28. July 2013).

[31] CAEN, http://caen.it (28. July 2013).

Acknowledgements

First of all, I would like to express my gratitude to Prof. Laura Fabbietti and Dr. Bernhard Ketzer for giving me this incredible opportunity, for their confidence in me and their help and support. I am most thankful to my supervisor Dr. Piotr Gasik for his patience, his constant support and his optimism that at some point just skipped over to me.

I would like to thank everyone from the Kaon Cluster Group, especially Martin Berger and Robert Münzer for their incredible help with software problems of any kind and Jacopo Margutti for his awesome support and the very fruitful discussions we had about whatever topic. Also I would like to thank all the other Bachelor students, especially Robert and Tobias. Thank you to Christoph Bilko and Daniel Heuchel for their work during the preparations for the test beam.

From E12, I would like to thank Dr. Roman Gernhäuser and Dr. Ludwig Meier for their incredible support and the new ideas they brought into this project.

I would like to express my gratitude to Dr. Walter Assman and his group, especially to Dr. Sabine Reinhardt who was a great help. I want to thank everyone of the MLL staff, especially Walter Carli and the beam operators Georg Anachorlis and Peter Ring for making this possible.

Special recognition goes out to my parents, for all their constant support, advice and belief. And most of all, I want to thank Steffi, my love, who has been incredibly patient, kind, loving and brilliant.